

Automated Subpixel Photobathymetry and Water Quality Mapping

Robert L. Huguenin, Mo Hwa Wang, Robert Biehl, Scott Stoodley, and Jeffrey N. Rogers

Abstract

New photobathymetry and water quality software is described here that utilizes subpixel analysis software (Subpixel Classifier) with an autonomous image calibration procedure and analytic retrieval algorithm to simultaneously retrieve and report bottom depth and the concentrations of suspended chlorophyll, suspended sediments, and colored dissolved organic carbon on a per-pixel basis from four-band multispectral image data. From the derived composition, the QSC2 (Quantitative Shoreline Characterization, Version 2.0) software also computes and reports water column visibility parameters (vertical and horizontal subsurface sighting ranges and turbidity, each at four wavelength band passes, plus Secchi depth as a scalar) as well as depth and turbidity confidence. QSC2 compensates for the effects of the atmosphere, sun and sky reflections from the water surface, subpixel contributions from exposed land, and variations in the bottom material properties. All information is derived automatically from the pixel data alone. The performance of the QSC2 software was demonstrated using a four-band Ikonos image of Plymouth, Massachusetts. Accuracies of the image-derived compositions, water clarity, and depths were assessed using field and laboratory measurements for eight representative lakes in the scene. The means of the differences of the field-measured and image-derived suspended chlorophyll and colored dissolved organic carbon concentrations for the eight lakes were 1.82 $\mu\text{g/l}$ and 4.34 mgC/l , respectively. The image-derived concentrations of suspended sediments were all below the threshold of detection for the field samples (5 mg/l), in agreement with the field data. The mean of the differences between field-measured and image-derived Secchi depths was 0.76 m. The mean depth difference was 0.57 m.

Introduction

Retrieval of bottom depth, water composition, and water clarity information from satellite and airborne multispectral imagery has been attempted with mixed success, particularly for near-shore and inland lake waters. Attenuation of light by suspended and dissolved materials complicated past algorithms for retrieval of bottom depth. Most photobathymetry applications have either been for relatively clear waters, or characteristics of the water column were approximated using independently characterized pixels of nearby deep waters (Polcyn *et al.*, 1970; Lyzenga, 1978; Lyzenga, 1981; Lyzenga, 1985; Clark *et al.*, 1987; O'Neill and Miller, 1989; Philpot, 1989; Walker *et al.*, 1990; Huguenin *et al.*, 1997b; Zhang *et al.*, 1999). Furthermore, the presence of reflected light from the bottom interferes with most empirical algorithms for retrieving the

properties of the water column. Consequently, most water column characterization applications have been for optically deep waters (Gordon *et al.*, 1988; Mausel *et al.*, 1991; Garver and Siegel, 1997; O'Reilly *et al.*, 1998; Carder *et al.*, 1999; Dierssen and Smith, 2000; Reynolds *et al.*, 2001; Ruddick *et al.*, 2001; Cipollini *et al.*, 2001; LaPotin *et al.*, 2001; Maritorena *et al.*, 2002).

Several factors affected past algorithm performance. These included incomplete model representations of bottom reflectance and water column optical attenuation characteristics; inadequate correction for surface reflections of sky radiance and sun glints; inadequate calibration for sun angle, atmospheric, and other environmental factors; and/or inadequate compensation for diverse and mixed bottom materials, among other factors. Attempting to compensate for these limitations, Lee *et al.* (2001) developed a semi-analytical model for shallow-water remote sensing using hyperspectral data and a model-driven optimization technique. They demonstrated that simultaneous retrieval of bottom depth and water column characteristics is indeed feasible for turbid shallow water cases. The simultaneously derived properties included bottom depth as a scalar, plus the spectra of bottom albedo, water absorption coefficients, and water backscattering coefficients. The spectra of water absorption coefficients and water backscattering coefficients were then fed into a model to derive the composition of the water column. Although accuracies of the retrieved parameters were not reported, the Lee *et al.* (2001) model was able to achieve reasonable agreement between retrieved depths and a NOAA chart and recent bathymetric survey. The retrieved chlorophyll concentrations were also in the range of a value measured at a nearby calibration site in their test image.

Although the Lee *et al.* (2001) model demonstrated that both bathymetric and water quality information can in principle be simultaneously retrieved from airborne spectral imagery, there is a need to be able to do this using commercially available multispectral sensors (e.g., Ikonos and Landsat Thematic Mapper). This is critical to meet data cost and availability (including historical coverage) requirements of water quality applications and to support rapid-response Naval operations requirements. Additional efficiency can also be gained if these retrievals can be achieved without the requirement for ground radiance measurements at calibration sites in the image, as required in the Lee *et al.* approach. This is critical for using archived and historical data, for supporting operations in denied or otherwise inaccessible areas, and for minimizing costs in water quality projects.

New photobathymetry and water quality software is described here that utilizes a different approach than that of

R.L. Huguenin, M.H. Wang, R. Biehl, and S. Stoodley are with Applied Analysis Inc., 630 Boston Road, Billerica, MA 01821 (rhuguenin@discover-aai.com).

J.N. Rogers is with GeoSyntec Consultants Inc., 629 Mass. Ave. Boxborough, MA 01719.

Photogrammetric Engineering & Remote Sensing
Vol. 70, No. 1, January 2004, pp. 111–123.

0099-1112/04/7001-0111/\$3.00/0
© 2004 American Society for Photogrammetry
and Remote Sensing

Lee *et al.* (2001). The QSC2 (Quantitative Shoreline Characterization, Version 2.0) software simultaneously retrieves four scalar parameters (bottom depth, and the concentrations of suspended chlorophyll, suspended sediments, and colored dissolved organic carbon) on a per-pixel basis, requiring only four-band multispectral data, rather than hyperspectral data. From the retrieved composition, QSC2 computes and reports water column visibility parameters (vertical and horizontal subsurface sighting ranges and turbidity, each at four wavelength band passes, plus Secchi depth as a scalar). It also performs an entirely autonomous calibration to reflectance, using only the image data, rather than requiring the use of MODTRAN (Moderate Resolution Transmittance Code, an atmospheric transmittance and radiance calculation model and code developed by the Air Force Research Laboratory, Space Vehicles Directorate, Hanscom AFB, Massachusetts) and the collection of ground radiance measurements at calibration sites. The accuracy of these automatically derived water quality parameters was assessed using commercially available, four-band Ikonos data that were provided by Space Imaging, Inc. A region was selected in Plymouth, Massachusetts that contained sufficient variability in lake characteristics (water quality/clarity, depth, bottom type, lake size, and vegetation cover) so as to make a challenging test case for the QSC2 software.

Approach

A special version of *Subpixel Classifier*, referred to as QSC2, was created to simultaneously retrieve water depth and water quality information from image pixels. *Subpixel Classifier* (available as a module within ERDAS IMAGINE) is a multispectral/hyperspectral image processing software module that detects spectral contributions from materials of interest that may occupy only small fractions of image pixels (Huguenin *et al.*, 1997a; Flanagan and Civco, 2001). It does this by identifying and removing unwanted spectral contributions from background materials in the pixels, and comparing the residual spectrum (after background removal) to a spectral signature for the material of interest. If the residual spectrum matches the signature spectrum (within an allowed tolerance), the pixel is designated as containing the material of interest. The process reports the fraction of the pixel containing the material (1.0 minus the fraction of background removed).

QSC2 takes advantage of the background suppression capabilities of *Subpixel Classifier* to detect and isolate the spectral contribution of water in image pixels even when it occupies only a fraction of a pixel. QSC2 uses a different environmental correction process than the one in *Subpixel Classifier*, however. It uses instead *Image Calibrator* to automatically convert the detected water spectrum to units of apparent reflectance, utilizing image data alone and requiring no ground truth or external information (Huguenin *et al.*, 1998). *Subpixel Classifier's* interactive Signature Derivation module is also not used in QSC2. Instead, it uses a new automated process, described below, which was embedded within the Classification module. Finally, it adds a post-processing module, also described below, to simultaneously retrieve the water depth and water quality information.

Automatic Signature Derivation

The signature derivation process in QSC2 is a three-step process. The first step utilizes a standard unsupervised classifier, ISODATA clustering, to classify the image into eight primary spectral classes. This is followed by a "cluster busting" step, classifying each primary class into eight subclasses. The second step categorizes the class/subclass spectra into "water classes" and "non-water classes." The eight primary class spectra and 64 subclass spectra are next converted to units of apparent reflectance using the output from *Image Calibrator*. Water classes/subclasses are then identified as those with

reflectances (at $\lambda > 0.75 \mu$) less than 0.1. The third step converts each water subclass spectrum (in original DN units) into a standard *Subpixel Classifier* signature using processes adapted from *Subpixel Classifier's* Signature Derivation module. The water subclass spectrum serves as the signature spectrum, $Sig(s,n)$, while randomly selected pixels from the subclass provide the necessary training data to establish the other two components of the *Subpixel Classifier* signature, namely, the spectral filters and intensity screen. Another signature, $Sig(p,n)$, is derived from the mean of the water primary class spectra and randomly selected training pixels from the full set of water pixels.

Water Detection

The pixels, $P(s,n)$, belonging to a particular water subclass, s , are processed to detect and isolate the water component, $W(n)$, using the signature, $Sig(s,n)$, for that sub-class only. Pixels belonging to the non-water subclasses are processed using $Sig(p,n)$.

The background removal process is a modified version of the standard process in *Subpixel Classifier*. The modification restricts the candidate backgrounds to non-water backgrounds. Otherwise, it is the same as the standard process. Each pixel spectrum, $P(n)$, is processed with the appropriate signature, $Sig(s,n)$ for the water subclass pixels or $Sig(p,n)$ for the non-water class pixels, to remove any subpixel non-water component (cloud or terrain), $B(n)$, that may be present.

$$W(n) = [P(n) - k_1 B(n)] / (1 - k_1) \quad (1)$$

where $W(n)$ is the detected water component of $P(n)$ and k_1 is the fraction of $B(n)$ in $P(n)$.

Retrieval of Water Depth and Composition

Central to the derivation of water depth and water quality information from the detected water spectrum, $W(n)$, is a four-dimensional reflectance look-up table (LUT). Water reflectance in four spectral bands is predicted for sequences of 50 depths and 50 concentrations each of suspended minerals, suspended chlorophyll, and dissolved organic carbon using the expression

$$R(n) = w(n)F(n)[b(n)/a(n)]\{1 - e^{-2c(n)z}\} + w(n)r(n)e^{-2c(n)z}. \quad (2)$$

Here, $R(n)$ is the reflectance of $W(n)$, exclusive of glint. The right hand side of Equation 2 represents the sum of the volume reflectance (first term), $R_{vol}(n)$, and bottom reflectance (second term), $R_{bot}(n)$, contributions to $R(n)$. The $w(n)$ term is the effective two-way air-water interface attenuation. $F(n)$ is a proportionality factor between the volume reflectance of the water column below the air-water interface and the ratio $b(n)/a(n)$, where $a(n)$ and $b(n)$ are the absorption and backscattering coefficients, respectively, of the water column. The $r(n)$ term represents the bottom reflectance, while $2c(n)$ is the effective two-path water column total attenuation coefficient, where $c(n) = a(n) + b(n)$, and z is depth. To populate the LUT, the product $w(n)F(n)$ was assigned a wavelength invariant value of $w(n)F(n) = 0.1735$. The basis for this is as follows.

The $w(n)$ term can be defined by the expression (Smith and Baker, 1986; Mueller *et al.*, 1995)

$$w(n) = t_r(n) * [1 - \rho(n,\theta)] / \eta^2(n). \quad (3)$$

Here $t_r(n)$ is the transmittance of the downwelling irradiance across the air-sea interface, estimated to be 0.96 at visible wavelengths (Smith and Baker, 1986; Dierssen and Smith, 1997). The Fresnel reflectance from water to air, $\rho(n,\theta)$, has been estimated to be 0.021 to 0.022 over the visible wavelength range (Dierssen and Smith, 2000). Using the standard index of refraction for water, $\eta(n)$, over the relevant wavelength and temperature ranges (Thormahlen *et al.*, 1985), this yields $w(n) = 0.515$ to 0.524, weakly dependent on wavelength. This is consistent

with conclusions and values derived from independent methodologies (Dierssen and Smith, 2000).

$F(n)$ in $w(n)F(n)$ includes the following: a factor $f(n)$ that relates apparent (measured) reflectance to inherent reflectance of the water column (Morel and Gentili, 1993); a factor $Q(n)$ that describes the anisotropy of the radiance distribution ($Q(n) = E_u(n)/L_u(n)$, where E_u is upwelling irradiance and L_u is the corresponding upwelling radiance) (Morel and Gentili, 1991; Morel and Gentili, 1993); and sun angle effects. Although there are wavelength dependencies in the constituent terms, $F(n)$ was found to be relatively invariant with respect to wavelength (Morel and Gentili, 1991; Morel and Gentili, 1993; Bukata *et al.*, 1995, pp. 92–102). There is some dependence of $F(n)$ on the magnitude of $b(n)/a(n)$ and solar incidence angle, however (Bukata *et al.*, 1995, pp. 92–102). Following the formalism of Gordon *et al.* (1975) for open ocean waters, Kirk (1984) performed Monte Carlo simulations to estimate $F(n)$ for more turbid waters, from which

$$F(n) = 0.975 - 0.629\mu_0 \quad (4)$$

where $\mu_0 = \cos(\theta_0)$, θ_0 being the refracted solar incident angle. Jerome *et al.* (1983) noted a second-order dependence of $F(n)$ on the backscattering probability, $\beta(n)$. Kirk (1991) investigated this further, leading to an expression for $F(n)$ dependent on both $\beta(n)$ and μ_0 (Bukata *et al.*, 1995, p. 101). Other expressions were developed by DiToro (1978) to address the complex scattering properties of turbid estuarine waters at low sun angles, leading to an expression that takes into account additional dependencies on sun angle. These latter effects, however, can generally be ignored for all but low sun angles. The Monte Carlo simulations were carried out at depth $z = 0$, i.e., just below the air/surface interface. $F(n)$ can be assumed to be invariant with depth as long as the water column is homogeneous. Using refracted solar incident angles representative of most commercially available sensor data, and neglecting the weak dependence on wavelength, $w(n)F(n) = 0.1735$ becomes a reasonable approximation.

The bottom reflectance term, $w(n)r(n)$, in Equation 2 has a default value that was derived empirically from a shallow-water Ikonos image of the Bahamas (where the water is nearly pure from an optical perspective). Errors in assumed $w(n)r(n)$ are at least partially compensated for by an empirical correction factor, $\gamma(s,n)$, described below. The user can optionally input alternative $r(n)$, or $w(n)r(n)$ can be derived from the image being processed.

The $a(n)$ and $b(n)$ terms in Equation 2 are defined as

$$a(n) = a_w(n) + C_{chl}a_{chl}(n) + C_{SM}a_{SM}(n) + C_{CDOC}a_{CDOC}(n) \quad (5)$$

and

$$b(n) = b'_w(n)\beta_w(n) + C_{chl}b'_{chl}(n)\beta_{chl}(n) + C_{SM}b'_{SM}(n)\beta_{SM}(n). \quad (6)$$

In these expressions, $a_w(n)$ and $b'_w(n)$ are the absorption and scattering cross sections, respectively, of pure water. The other terms, $a_i(n)$ and $b'_i(n)\beta_i(n)$, are the known absorption and backscattering cross-section spectra, respectively, of other aquatic components suspected to be in the water column. Note that the backscattering cross section for each component is explicitly expressed as the product of the scattering cross section, $b'_i(n)$, and backscattering probability, $\beta_i(n)$, for that component. C_{chl} , C_{SM} , and C_{CDOC} are the concentrations of suspended chlorophyll, suspended minerals, and chromophoric dissolved organic carbon, respectively. Numerous suspended and dissolved constituents can exist within the water column, and the chemistry can be quite complex. However, not all of the constituents are optically significant. Typically, only a few components affect the volume reflectance of a water mass, even under complex chemistry conditions (*c.f.*, Bukata *et al.*,

1981). From an optical point of view, the water mass can be considered a combination of pure water, a suspended organic component, a dissolved organic component, and a suspended inorganic component. For most waters, the optically dominant suspended organic component is chlorophyll (in the form of chlorophyll a + phaeophytin). The optically dominant suspended inorganic component is typically in the form of suspended minerals. The optically dominant dissolved organic matter component is the melanoid-colored fraction, i.e., the fraction produced by the Maillard reaction (Kalle, 1966), typically amounting to about 10 to 40 percent of the total dissolved organic matter concentration (Bukata *et al.*, 1995, p. 123). Although this may be an over-simplification of the state of the water body, this four-component optical model is generally sufficient to describe the volume reflectance characteristics of most inland and coastal waters (*c.f.*, Bukata *et al.*, 1981; Bukata *et al.*, 1995, p. 105).

The effective two-path water column total attenuation coefficient, $jc(n)$, is approximated using $j = 2$ in Equation 2. The j term is highly complex, but it can be approximated by $j = [1/\cos(\theta_w)] + [D_u^B/\cos(\theta_v)]$ (Lee *et al.*, 1999), where θ_w and θ_v are the subsurface solar zenith angle and subsurface viewing angle from nadir, respectively; $D_u^B \approx 1.04[1 + 5.4u(n)]^{0.5}$; $u(n) = b(n)/[a(n) + b(n)]$; and $a(n)$ and $b(n)$ are the absorption and backscattering coefficients, respectively, of the water column. For most water compositions and viewing geometries, $j \approx 2$, which is also consistent with the assumption of Walker *et al.* (1990).

Equations 2, 5, and 6 served as the governing equations for populating the LUT using the various combinations of z , C_{chl} , C_{SM} , and C_{CDOC} . To simultaneously retrieve these four parameters from the detected water spectra, $W(n)$, an additional factor, $\gamma(s,n)$, is needed. Because $w(n)r(n)$, $w(n)F(n)$, glint contributions, and other properties controlling $W(n)$ can be different from those in the LUT, an empirical correction is autonomously derived to partially compensate for these combined differences. For each water subclass signature, $Sig(s,n)$, a signature-specific spectrum, $SUN_{LUT}(s,n)$, is derived: i.e.,

$$SUN_{LUT}(s,n) = SUNFACTOR(n) * \gamma(s,n). \quad (7)$$

$SUN_{LUT}(s,n)$ is then used in place of $SUNFACTOR(n)$ from *Image Calibrator* to convert detected water spectra to reflectance for use with the LUT: i.e.,

$$R_{LUT}(s,n) = [W(s,n) - ARAD(n)]/SUN_{LUT}(s,n). \quad (8)$$

To derive $SUN_{LUT}(s,n)$, $Sig(s,n)$ for class s is first converted to reflectance using the two environmental correction spectra from *Image Calibrator*.

$$R(s,n) = \{[Sig(s,n) - ARAD(n)]/SUNFACTOR(n)\} - p_{surf} \quad (9)$$

For each $R(s,n)$, the composition and depth is derived from the LUT; and the actual LUT reflectance, $R_{LUT}(s,n)$, for that depth and composition is retrieved from the LUT. The ratio of $R_{LUT}(s,n)$ to $R(s,n)$ then defines $\gamma(s,n)$ in Equation 7. The p_{surf} term is explicitly determined and removed from bands based on the reflectance values for bands with center wavelengths longer than 0.75 μm , when available (e.g., Landsat Thematic Mapper). Otherwise, it is implicitly removed through use of $\gamma(s,n)$ with the discrete LUT.

Water Clarity Characterization

Once $a(n)$ and $b(n)$ are known, additional water clarity information is derived and reported for each water detection. This includes the vertical and horizontal subsurface sighting ranges

$$VSSR(n) = 4.605/[1.4a(n) + 0.03b'(n)] \quad (10)$$

and

$$HSSR(n) = 4.605/[a(n) + b'(n)]. \quad (11)$$

Subsurface sighting range is defined here as the distance over which reflected radiance is attenuated to 0.01 of its starting value. Equation 10 is based on the Beer's Law expression for attenuation of irradiance, $E(n,z) = E(n,0)\exp[-k(n)z]$, for $E(n,z)/E(n,0) = 0.01$ and a vertical attenuation coefficient of $k(n) = 1.4a(n) + 0.03b'(n)$ (Pickard and Emery, 1982, p. 104), with $b'(n)$ being the scattering coefficient, not the backscattering coefficient. Equation 11 is based on the same Beer's Law expression, but substituting the total attenuation coefficient, i.e., $c(n) = a(n) + b'(n)$, for the vertical attenuation coefficient (Pickard and Emery, 1982, p. 104).

$VSSR(n)$ is directly analogous to the traditional field-measured Secchi depth parameter. Secchi depth represents the depth at which a submerged disk, viewed from above the air-water interface, loses contrast with the background. Like $VSSR(n)$, Secchi depth generally corresponds to the depth where $E(n,z)/E(n,0) = 0.01$ (Bukata *et al.*, 1988). The principal distinction between the two is the position of the observer: $VSSR(n)$ is from a vantage point below the air-water interface, while Secchi depth is measured from above. Secchi depth can be estimated from the total attenuation coefficient reported by QSC2. Bukata *et al.* (1988) derived empirical relationships between Secchi depth (S) and total attenuation coefficient (c = total attenuation coefficient integrated over the visible wavelength range) for several bodies of water (five of the Great Lakes) covering the range $0.5 \text{ m} \leq S \leq 20 \text{ m}$. The results took the form of $c = A(S^{-1})^B$, where A and B were constants derived from regression analyses. There were differences between lakes, with A ranging from 2.85 to 5.85 and B ranging from 0.8 to 1.0. Correlation coefficients were high, however (0.98 to 0.99). Using the means of A and B for the five lakes, and transforming the expression into S as a function of c , one can obtain the following first-order estimate for Secchi depth:

$$S = (4.30/c)^{1.08}. \quad (12)$$

Here c is the mean of $c(n)$ across the visible wavelength range. Comparison of Equations 11 and 12 with $c(n) = a(n) + b'(n)$ reveal that Secchi depth is generally comparable in magnitude to the mean of $HSSR(n)$ over the visible wavelength range: $S = 0.928 HSSR^{1.08}$. Note that the field-measured Secchi depth is a qualitative parameter, dependent on the perception and experience of the observer. Also, because it involves lowering a disk into the water, it can only be measured in the field when Secchi depth is less than actual depth. In contrast, S from Equation 12 is quantitatively derived from the three image-derived concentrations, and it is therefore not as qualitative and it is not restricted to depths less than the actual depth.

Another water clarity parameter reported by the software is turbidity. Generally, turbidity refers to the amount of attenuation by particulate scattering in the water, usually expressed in Nephelometric Turbidity Units (NTU). However, there is not a universally accepted quantitative relationship between the concentration of particulates and NTU units. The off-axis NTU measurement geometry utilizes particulate scattering in a way that includes attenuation by both absorption and scattering when particulates are present, but it reports below-threshold attenuation when particles are not present. Because of the inclusion of the effects of absorption in the attenuation measurement, the NTU units cannot be used to derive particle concentration. As an alternative to NTU, one can instead use the definition of turbidity adopted by Pickard and Emery (1982, p.104), namely, turbidity = total attenuation coefficient, $c(n)$. The QSC2 software reports turbidity as $c(n)$ rather than NTU. NTU and $c(n)$ are comparable indicators of

water clarity when particulates are present. Because of the difference in measurement geometry, however, $c(n)$ values may not be good indicators of turbidity when particulate concentrations are low, e.g., in low-particulate waters containing appreciable concentrations of colored dissolved organic carbon (CDOC).

In addition, turbidity confidence and depth confidence values are reported for each pixel, providing a means for identifying compositional, visibility, and depth errors caused by uncompensated errors in the model assumptions. The accuracies of the reported depth and water quality parameters can vary from pixel to pixel due to a variety of factors. These can include uncompensated differences in bottom materials, surface reflectance, etc. They can also include anomalous materials in the water column. Turbidity confidence is

$$C_T = 1 - f \quad (13)$$

where f is the least-squares fit value between $R_{LUT}(s,n)$ and $R(s,n)$. Depth Confidence is

$$C_D = 1 - f \quad \text{for } 0.25 \text{ m} \leq z \leq 1.5 * S \\ = 0 \quad \text{for } z < 0.25 \text{ m, or } z > 1.5 * S \quad (14)$$

where S is the image-derived Secchi depth, defined by Equation 12. The two limits in Equation 14 reflect a problem inherent in the LUT approach, namely, the potential for multiple solutions. The problem is most acute when the bottom does not contribute to pixel reflectance, i.e., when z is greater than $1.5 * S$. When this occurs, z is frequently reported as anomalously shallow (z less than 0.25 m); hence, the two limits in Equation 14. The multiple solution problem can potentially manifest itself in one or more of the derived parameters other than depth. In that case, the correct solution can be assumed to be the one closest to the signature's derived parameter values.

QSC2 Accuracy Assessment

The accuracy of QSC2 was assessed using an Ikonos image and field sample data for a portion of Plymouth harbor and a set of nearby inland lakes in southeastern Massachusetts. The image, acquired on 30 August 2001 as part of GeoSyntec Consultant's NASA funded ARC Project with Brown University, was a four-band multispectral product with 4-m GSD pixels, resampled in nearest-neighbor format. The image is shown in Plate 1.

Ground Truth Field Data

Field data were acquired at sites in numerous inland lakes in the image to assess the accuracy of the image-derived results. The locations and names of the lakes in which field samples were acquired are shown in Plate 1. Field data and samples were acquired from canoes by qualified GeoSyntec field staff on several dates between June and August, 2001.

The date, time, location (GPS UTM coordinates), and local weather conditions for each *in situ* measurement and water sample collection were recorded. Field data included *in situ* measurements of water temperature, turbidity (Nephelometric Turbidity Units), Secchi depth (meters), actual depth (meters), specific conductivity (micromhos/cm), dissolved oxygen (mg/l), pH, and Oxygen Reduction Potential (mV). Water samples were collected near the surface and analyzed in the laboratory by Alpha Analytical Labs of Westborough, Massachusetts at the direction of GeoSyntec. Laboratory analyses included measurements of total phosphorous (mg/l), Chlorophyll *a* ($\mu\text{g/l}$), turbidity (NTU), dissolved organic carbon (mgC/l), total suspended solids (mg/l), and NO_3/NO_2 (mg/l).

The sampling stations were identified using the DGPS coordinates recorded at the field sites. The image was projected into the UTM WGS-84 projection, and the accuracy of pixel locations was estimated to be within 12 m (horizontal). Because

of the locational uncertainty, field-measured depths and water quality data were compared to the mean image-derived values for 3- by 3-pixel clusters, centered on the registered location.

Depth

The image-derived depths for the various water bodies in the image are illustrated in Plate 2a. In Plate 2b, the depths for the harbor area are compared to a USGS topographic map for the same area (depth in feet). The image-derived depths in the harbor are in good general agreement with the depths on the map, but there is significantly more detail in the image map not available from the topographic map or the corresponding nautical chart (not shown). A comparison of image-derived depths to field-measured depths is presented in Table 1 for eight representative inland lakes. All image-derived depths are included in the plates and table, although only three of the depths in the table passed the valid-depth filter ($0.25 \text{ m} < \text{depth} < 1.5 \text{ S}$).

Differences between the field-measured and image-derived depths for the three valid measurements ranged from 0.03 m to 1.29 m, with a mean of 0.57 m. A comparison of the field-measured depths in Table 1 to field-measured Secchi depths (Table 5) reveal that the actual depths were less than 1.5 times the field-measured Secchi depths for only two of the three "valid" stations ("Muddy" and "Lwest"). The bottom would only have been visible at these latter two stations. Depths were underestimated by 0.03 m and 0.38 m, respectively, yielding a mean error of 0.21 m at these locations. At the third site ("Bwest"), actual depth was more than twice the field-measured Secchi depth, while the image-derived depth was very close to the image-derived Secchi depth, erroneously allowing it to pass the filter. The field-measured depths at the other five sample stations were all greater than 1.5 times the field-measured Secchi depth, and they were thus correctly identified as having invalid depths.

Water Composition

Plate 3 presents the concentrations of suspended chlorophyll (left), suspended sediments (center), and colored dissolved organic matter (right). Comparison of the patterns of derived concentrations in Plate 3 with depth (Plates 2a and 2b) reveals little or no evidence of any unwanted depth dependencies of the concentrations.

Suspended Chlorophyll

Quantitative comparisons of the image-derived concentrations with the field-measured concentrations for the same lake sites listed in Table 1 are presented in Tables 2, 3, and 4. Table 2 illustrates the concentrations of suspended chlorophyll a for the same sites listed in Table 1. The mean of the differences between the image-derived and field-measured chlorophyll concentrations for the complete set of eight sample stations is $1.82 \mu\text{g/l}$. In contrast, the mean difference for the three sample

TABLE 2. COMPARISON OF IMAGE-DERIVED AND FIELD-MEASURED CONCENTRATIONS OF SUSPENDED CHLOROPHYLL A ($\mu\text{g/L}$) AT SAMPLED INLAND LAKE LOCATIONS IN THE PLYMOUTH HARBOR IMAGE

Station	Date	Image-Derived	Field-Measured	Difference
Stri	26 Jun 01	0.70	1.14	-0.44
Smelt	22 Aug 01	5.84	1.90	+3.94
Muddy	29 Aug 01	1.59	0.99	+0.60
Micajah	28 Jul 01	1.04	2.90	-1.86
Lwest	28 Jul 01	2.04	2.7	-0.66
Cooks	22 Aug 01	0.96	1.17	-0.21
Bwest	28 Jul 01	6.61	4.30	+2.31
BillSea	13 Aug 01	16.63	12.20	+4.43

stations having valid depths ("Muddy," "Lwest," and "Bwest") is $1.23 \mu\text{g/l}$ while, for the two samples actually having a visible bottom ("Muddy" and "Lwest"), it is $0.70 \mu\text{g/l}$. This suggests that the image-derived concentrations of suspended chlorophyll may potentially have been adversely affected by the errors in depth calculation for the cases in which the bottom is not visible. However, other factors may have also contributed.

First, the water sample represents a small volume (≤ 1 liter) that may not be representative of the much larger volume represented by the 3- by 3-pixel (144-m^2 area) mean. This is particularly true if the water body is horizontally and/or vertically heterogeneous. Also complicating the assessment of accuracy is the fact that the dates of field sampling did not coincide with the date of image acquisition. Chlorophyll concentration in lakes not only varies with season but can also vary with changes in temperature, hours of sunlight, and nutrient levels. An example of this can be observed at the Billington Sea sampling station. This location was sampled on six dates (26 June 2001, 12 July 2001, 28 July 2001, 13 August 2001, 22 August 2001, and 29 August 2001), during which period the sampled chlorophyll a concentrations progressively increased from 5.12 to $37.20 \mu\text{g/l}$. The corresponding image-derived values at these five Billington Sea sampling stations, all measured simultaneously from the Ikonos imagery on 30 July 2001, revealed much less variation, ranging from 13.39 to $17.78 \mu\text{g/l}$ with a mean of $16.07 \mu\text{g/l}$. This suggests that the variations in the Billington Sea field samples were more temporal than spatial. The differences in Table 2 could thus also be due in part to temporal differences in chlorophyll concentration between the dates of sampling and image acquisition (30 July 2001).

Suspended Minerals

The image-derived concentrations of suspended sediments are listed in Table 3 for the same eight sample locations as in

TABLE 1. COMPARISON OF IMAGE-DERIVED AND FIELD-MEASURED DEPTHS (METERS) FOR EIGHT REPRESENTATIVE INLAND LAKE LOCATIONS IN THE PLYMOUTH HARBOR IMAGE. FIELD MEASUREMENT ACCURACIES WERE TO 0.1 METER

Station	Date	Image-Derived	Field-Measured	Difference
Stri	26 Jun 01	(5.41)	5.00	n/a
Smelt	22 Aug 01	(7.64)	4.80	n/a
Muddy	29 Aug 01	4.97	5.00	-0.03
Micajah	28 Jul 01	(8.89)	8.00	n/a
Lwest	28 Jul 01	4.02	4.50	-0.48
Cooks	22 Aug 01	(5.34)	3.80	n/a
Bwest	28 Jul 01	2.51	3.80	-1.29
BillSea	13 Aug 01	(0.16)	2.30	n/a

TABLE 3. COMPARISON OF IMAGE-DERIVED SUSPENDED SEDIMENTS (MG/L) AND FIELD-MEASURED TOTAL SUSPENDED SOLIDS (MG/L) CONCENTRATIONS AT SAMPLED INLAND LAKE LOCATIONS IN THE PLYMOUTH HARBOR IMAGE [5 MG/L DETECTION LIMIT, ND (NON DETECT), AND NS (NOT SAMPLED)]

Station	Date	Image-Derived	Field-Measured
Stri		5.10	NS
Smelt	22 Aug 01	2.47	ND
Muddy	29 Aug 01	2.19	ND
Micajah		1.69	NS
Lwest	29 Aug 01	1.77	ND
Cooks	29 Aug 01	3.22	ND
Bwest		2.41	NS
BillSea	22 Aug 01	2.78	ND

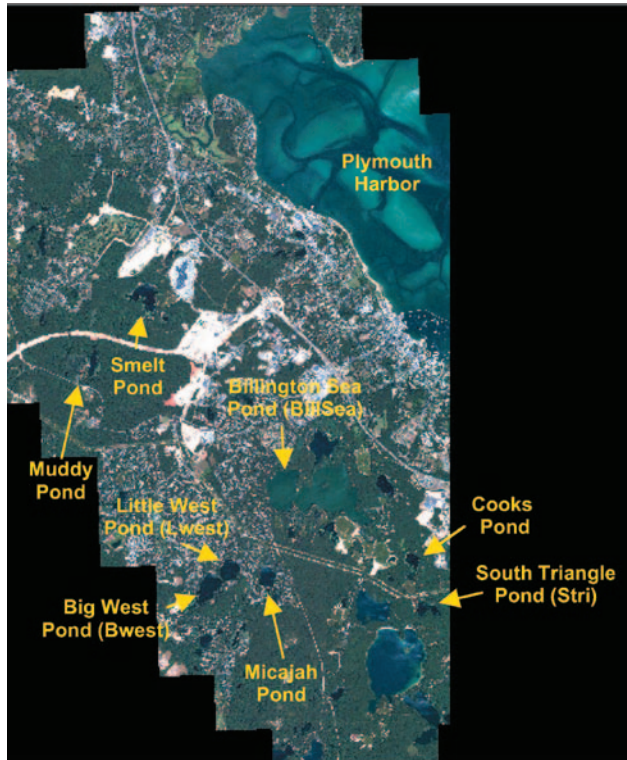


Plate 1. Ikonos image, acquired on 30 July 2001, of Plymouth Harbor and a set of nearby inland lakes in southeastern Massachusetts. The names of the lakes for which field data were acquired are indicated.

measured concentrations of dissolved organic carbon (DOC). The two concentrations are not directly comparable; therefore, comparison of the two concentrations has to be done with considerable caution. The field-measured concentrations are from sample filtrates, using a 0.45- μm filter, that were analyzed for dissolved organic carbon using a high-temperature combustion analysis procedure. In contrast, the image-derived CDOC concentrations represent the concentration of carbon in the yellow and brown melanoid portion of the dissolved organic matter, i.e., the colored fraction produced by the Mailard reaction.

Note that the image-derived values in Table 4 are consistently higher than the field-measured values. The mean of the differences for the eight sample stations is 4.34 mgC/l, which is comparable to the mean of the differences for the three sites having valid depths (5.0 mgC/l). This suggests that the image-derived concentrations of CDOC were probably not noticeably affected by any bottom contribution to pixel radiance.

The origin of the differences between the field sample and image-derived concentrations is uncertain. One possibility is that the differences are due to the differences in sampling characteristics. The field samples were collected near the surface, while the image-derived values are vertically integrated to depths of 1.2 to 6 m, depending on the Secchi depth. In the absence of significant circulation and mixing, dissolved organic matter can potentially develop vertical concentration gradients that could either enhance or depress concentrations near the surface relative to the vertically integrated concentrations. In areas of high primary production, for example, a major source of dissolved organic carbon is production by algae degradation (autochthonic DOC). Because photosynthetic algae tend to be more concentrated near the surface, concentrations of dissolved organic matter in areas of high primary production can be enhanced near the surface. Conversely, in areas of low primary production, dissolved organic carbon concentrations can be suppressed near the surface as a result of egesta assimilation by the algae (Bukata *et al.*, 1995, p. 123). The chlorophyll concentrations in Table 2 are generally low in all but the Billington Sea sample. This suggests the possibility that, at most of the sample stations, primary production may also have been low, and, consequently, that surface DOC concentrations (where the sampling occurred) may have been suppressed relative to the vertically integrated column concentrations. This could also have been true at the Billington Sea site, in spite of the relatively high concentrations of chlorophyll there.

Water Clarity

QSC2 reported four indicators of water clarity, derived from the retrieved composition. $VSSR(n)$ and $HSSR(n)$ were reported for four wavelength ranges corresponding to the Ikonos sensor band passes for Band 1 (445 to 516 nm), Band 2 (506 to 595 nm), Band 3 (632 to 698 nm), and Band 4 (757 to 853 nm). The other two reported water clarity parameters included turbidity (total attenuation) for the same four band passes and an estimate of Secchi depth.

$VSSR(n)$

Plate 4 (left) shows the Vertical Subsurface Sighting Range output plane for the Band 1 band pass. Output planes for the Bands 2, 3, and 4 band passes are not shown in this table. This is because $VSSR(n)$ for the Bands 1, 2, and 3 band passes have very similar patterns to the output plane in Plate 4, differing only in magnitude. The $VSSR(n)$ output plane for the Band 4 band pass is not shown because the spatial variation is smaller than the bin size (1.2 to 1.5 m) and it has no visible structure. The $VSSR(n)$ ranges do differ across the various band pass ranges, however, as seen in the histograms for the various bands in Plate 4 (right).

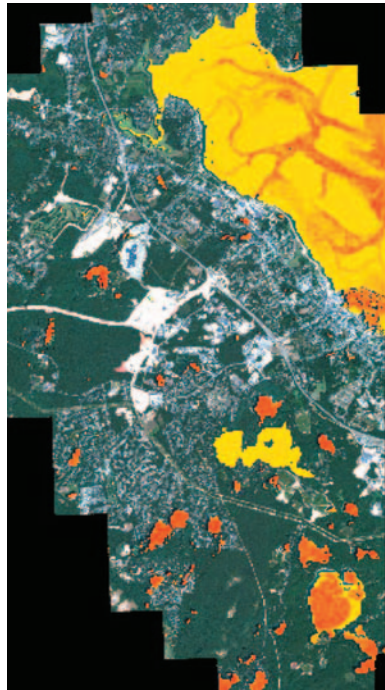
Tables 1 and 2. TSS was measured by traditional gravimetric analysis for only four of the samples in Table 3. Sediment concentrations for each of four samples were below the detection threshold (5 mg/l). Of the 15 total field samples analyzed for TSS (only four of which are included in Table 3), only one yielded a value at the detection threshold. That sample, drawn from the Billington Sea on 29 August 2001, yielded a field-derived value of 5 mg/l, which was close to the detection threshold and to the image-derived value for that location (not reported in Table 3) of 5.48 mg/l. For the four samples that were analyzed, the image-derived concentrations were in each case significantly below the 5 mg/l detection threshold, consistent with the non detect (ND) reports for these samples.

Dissolved Organic Carbon

Table 4 reflects the image-derived concentrations of colored dissolved organic carbon (CDOC) as compared to the field-

TABLE 4. COMPARISON OF IMAGE-DERIVED COLORED DISSOLVED ORGANIC CARBON (MGC/L) AND FIELD-MEASURED CONCENTRATIONS OF DISSOLVED ORGANIC CARBON (MGC/L) AT SAMPLED INLAND LAKE LOCATIONS IN THE PLYMOUTH HARBOR IMAGE

Station	Date	Image-Derived	Field-Measured	Difference
Stri	26 Jun 01	6.39	3.80	2.59
Smelt	22 Aug 01	7.29	3.00	4.29
Muddy	29 Aug 01	8.80	3.00	5.80
Micajah	28 Jul 01	5.72	1.50	4.22
Lwest	28 Jul 01	7.78	3.70	4.08
Cooks	22 Aug 01	7.89	2.90	4.99
Bwest	28 Jul 01	8.62	3.70	4.92
BillSea	13 Aug 01	7.24	3.60	3.64



Depth (m)

0.00000 - 0.19927	Yellow
0.19927 - 0.31594	Yellow
0.31594 - 0.50091	Yellow
0.50091 - 0.79418	Yellow-Orange
0.79418 - 1.25916	Orange
1.25916 - 1.99636	Orange
1.99636 - 3.16516	Orange-Red
3.16516 - 5.01828	Red-Orange
Over 5.01828 m	Red

(a)



(b)

Plate 2. (a) Image-derived depths for the Plymouth Harbor image shown in Plate 1. (b) Image-derived depths for the Harbor portion of the image compared to depths (feet) from a USGS topographic map of the same area.

The patterns in the $VSSR(n)$ output plane in Plate 4 represent variations in water clarity due to variations in the concentrations of the suspended chlorophyll, suspended sediments, and/or colored dissolved organic carbon in the pixel water column. Comparisons to the compositional maps in Plate 3 can be used to determine which constituents are primarily responsible for the variations in water clarity at any location of interest in the image.

Examination of the histograms in Plate 4 reveals that $VSSR(n)$ generally decreased with increasing wavelength. This reflects a progressive increase in light attenuation toward the longer wavelengths, which is consistent for waters containing low to moderate concentrations of suspended chlorophyll, dissolved organic carbon, and suspended sediments. There is also a generally progressive decrease in the spread of histogram values in Plate 4 with increasing wavelength. The

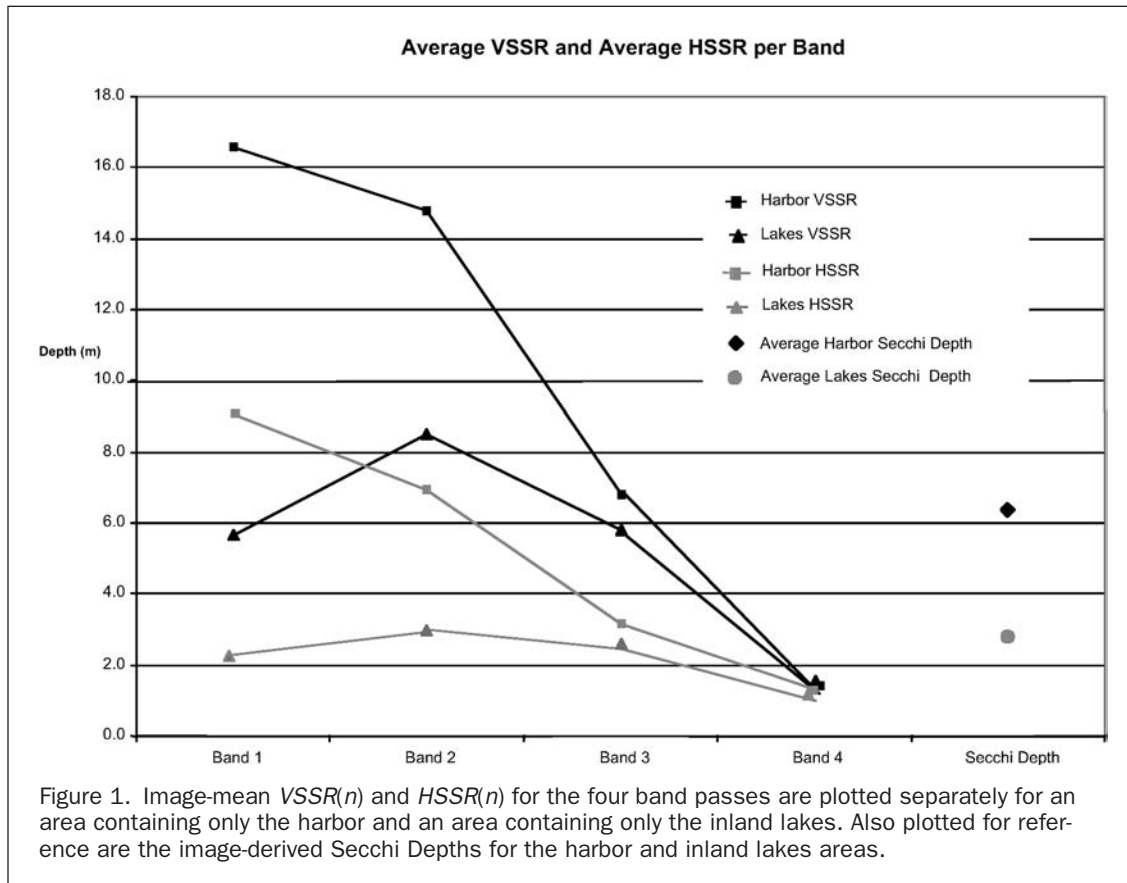


Figure 1. Image-mean $VSSR(n)$ and $HSSR(n)$ for the four band passes are plotted separately for an area containing only the harbor and an area containing only the inland lakes. Also plotted for reference are the image-derived Secchi Depths for the harbor and inland lakes areas.

reason for this spread can be seen in Figure 1, where the mean of $VSSR(n)$ for the four band passes is plotted separately for an area containing only the harbor and an area containing only the inland lakes. The two $VSSR(n)$ plots reflect two very different compositional characteristics for the harbor and inland lakes, progressively converging with increase in wavelength. The histograms in Plate 4 are for the image as a whole, and the spread in values reflect the divergence for the two classes of water seen in Figure 1.

HSSR(n)

Plate 5a (left) presents the Horizontal Subsurface Sighting Range output plane for the Band 1 band pass. The histograms for the Bands 1 through 4 band passes are shown on the right. Note that the patterns are generally similar to those in the $VSSR(n)$ output plane in Plate 4. $HSSR(n)$ is less than $VSSR(n)$ due primarily to the increased contribution from optical scattering by suspended materials in $HSSR(n)$ (Equation 10 versus 11). Like $VSSR(n)$, the sequence of image-mean $HSSR(n)$ over the four band passes for the harbor is different from that of the lakes, showing a progressive convergence with increasing wavelength. This can be seen in Figure 1, where image-mean $HSSR(n)$ for the four band passes is plotted for the harbor and inland lakes areas.

Turbidity

In Plate 5b, turbidity is shown in the output plane for the Band 1 band pass. The histograms for the Bands 1 through 4 band passes are shown on the right. Note that the patterns are generally similar to those in the $VSSR(n)$ and $HSSR(n)$ output planes in Plates 4 and 5b, respectively.

Secchi Depth

In Table 5 the image-derived Secchi depths are compared to the field-measured Secchi depths for the same eight field

TABLE 5. COMPARISON OF IMAGE-DERIVED AND FIELD-MEASURED SECCHI DEPTHS (BOTH IN METERS) AT EIGHT REPRESENTATIVE SAMPLED INLAND LAKE LOCATIONS IN THE PLYMOUTH HARBOR IMAGE. FIELD MEASUREMENT WAS TO 0.1 METER, BUT IT IS A SUBJECTIVE PARAMETER

Station	Date	Image-Derived	Field-Measured	Difference
Stri	26 Jun 01	2.0	3.0	-1.0
Smelt	22 Aug 01	2.7	3.5	-0.8
Muddy	29 Aug 01	3.5	4.5	-1.0
Micajah	28 Jul 01	4.6	6.0	-1.5
Lwest	28 Jul 01	3.8	3.2	+0.6
Cooks	22 Aug 01	2.8	3.2	-0.4
Bwest	28 Jul 01	2.5	1.8	+0.7
BillSea	13 Aug 01	1.5	1.2	+0.3

sample stations included in the previous tables. The differences between the image-derived and field-measured values are also included. With the exception of Micajah Pond, the image-derived and field-measured Secchi depths agree to within a meter. Indeed, the mean of the differences for the eight sample stations is 0.76 m. This is comparable to the mean of the differences for the three sites having valid depths (0.70 m), suggesting that the image-derived Secchi depths were probably not noticeably affected by bottom contribution to pixel radiance.

The origin of the differences between the image-derived and field-measured Secchi depths in Table 5 is uncertain, but it appears to be due at least in part to the differences between the two measurement approaches. Field-measured Secchi depth is a subjective parameter that depends on the overhead radiance characteristics, surface roughness, contrast of the Secchi disk against the background, and experience of the

observer. The image-derived value is calculated from the total attenuation coefficient derived from the retrieved composition, and it does not include the spectral transfer function for the photopic human eye. If the differences between the image-derived and field-measured Secchi depths in Table 5 were due primarily to errors in retrieved composition, it would be expected that there would be a correlation of the Secchi depth differences in Table 5 with either the compositions or the compositional differences in one or more of Tables 2, 3, and 4. None of the compositional parameters in Tables 2, 3, and 4 have patterns that correlate with the differences in Table 5, however. This suggests that the differences in Table 5 could be due primarily to the differences in measurement approach.

Comparison to QSC1

QSC2 was designed to improve some of the limitations of an earlier version of the software (QSC1). QSC1 was based on the same radiative transfer foundation as the QSC2 software described here. A principal difference is that the earlier version required interactive user development of signatures based on “ground truth” information for the depth calculations. The number of required signatures depended on the variety of water quality conditions and bottom types in the image. The depth calculation process was described by Huguenin *et al.* (1997b). QSC1 retrieved water composition and water clarity using a separate formula, described below.

With QSC1, water quality information could be retrieved only for deep water (depths greater than 1.5 Secchi depth). The user needed to have some knowledge of the water quality characteristics of the visibly darkest water, $W(0,n)$, in the image. The user interactively selected a “water quality category” for that water. The choices included “Ocean,” “Coastal,” and five inland trophic status classes (Ultra-Oligotrophic, Oligotrophic, Mesotrophic, Eutrophic, or Hypereutrophic). Each of these categories had a standard model composition (C_{so} , C_{si} , and C_d) and a corresponding computed volume reflectance spectrum, $R_{vol}(0,n)$. $R_{vol}(n)$ for the water detection, $W(n)$, was then computed using the expression

$$R_{vol}(n) = [W(n)/W(0,n)] * R_{vol}(0,n). \quad (15)$$

The composition for the water detection was then determined from $R_{vol}(n)$ using a three-dimensional pre-computed LUT approach, similar to the four-dimensional LUT used for QSC2. From the derived composition, the various water clarity parameters ($VSSR(n)$, $HSSR(n)$, and turbidity at three wavelengths, as well as depth confidence and turbidity confidence values) were computed and reported, as for QSC2.

A primary limitation of the water quality retrieval process in QSC1 is that the water quality characteristics of $W(0,n)$ are not always known. A second limitation is that errors due to bottom contribution for shallow water can significantly degrade the accuracies of the retrieved depth and water quality parameters. The water quality results from the original version were reasonably accurate, however, when the user had a reasonable knowledge of the trophic status of the darker waters, and bottom reflectance did not contribute appreciably to the upwelling radiance. By running the process in conjunction with the depth calculation model, the user could flag as potentially in error pixels having reported depths less than 1.5 S or Turbidity Confidence values below a threshold value (0.8).

A comprehensive evaluation of depth accuracy of the earlier QSC1 software was carried out by the Naval Oceanographic Office (Remote Sensing Division, Integration and Technology Department, located at Stennis Space Center, Mississippi) at the request of the Advanced MASINT Branch of the National Air Intelligence Center/DXDA (Wright Patterson Air Force Base, Ohio). Details of this independent assessment

and findings are available (on a need-to-know basis) from the Naval Oceanographic Office. The results are briefly summarized here.

The Navy test used Landsat Thematic Mapper imagery of study sites in California, Florida, North Carolina, and the Bahamas. Hydrographic surveys were conducted at each study site to provide sea truth for comparison to the bathymetric maps generated by the software. The analysis was complicated by the fact that precise depths were not provided as output from QSC1. Instead, the software binned depths into 15 discrete depth classes, having depth ranges that progressively increased with depth from ± 0.3 meter at a 0.3-meter depth to ± 3.2 meters at a 21.8-meter depth. An additional depth class included all reported depths greater than 25 meters. The hydrographic data were compared to the software output for the pixels collocated with the coordinates of the sea truth measurements. If the known depth fell within the reported depth class range at that location, the difference was recorded as zero. If the known depth fell outside of the classification range, the accuracy was determined by subtracting from the known depth either from the upper or lower limit of the range, depending on which calculation yielded the smaller result in an absolute sense. This resulted in an underestimate of errors.

The differences between the reported depths and sea truth were compiled to generate a mean and standard deviation. Means and standard deviations of errors for the four study areas were comparable. One of the study areas (6101 measurements) had a mean difference of -0.78 meters and a standard deviation of 1.9 meters. A second study area (1781 measurements) also had a mean difference of -0.78 meters and a standard deviation of 1.1 meters. A third area (1364 measurements) had a mean difference of $+0.82$ meters and a standard deviation of 0.99 meters. The fourth study area (1645 measurements) had a mean difference of $+0.99$ meters and a standard deviation of 2.1 meters. Factors that contributed to the differences were reported by the Navy to be poor satellite data quality, turbid water, heterogeneous atmospheric conditions, and inadequate sampling. Although a much smaller sample set, the depth differences reported for the Plymouth Harbor image using the QSC2 software were generally smaller than the differences reported using the earlier QSC1 version of the software.

A separate assessment of water composition performance using the earlier QSC1 software was done as part of the NASA Hyperspectral EOCAP project. A detailed description is provided by Karaska *et al.* (2004). This NASA-sponsored study attempted to see if the QSC1 software could be used with AVIRIS imagery to predict harmful algae blooms in the Neuse River estuary in North Carolina. Nearly all of the water in the estuary was optically deep, and trophic status could be estimated with reasonable certainty. Consequently, the application was well suited to the requirements for QSC1. It was found that the image-derived measurements of suspended chlorophyll correlated well with field measurements ($r = 0.84$). The AVIRIS measurements of suspended minerals, colored dissolved organic carbon, and turbidity, however, could not be quantitatively evaluated, because of limitations of the field data. The reader is referred to Karaska *et al.* (2004) for detailed descriptions of the compositional accuracy assessment and Algae Production Potential Index (APPI) derived from the compositional output planes.

Discussion

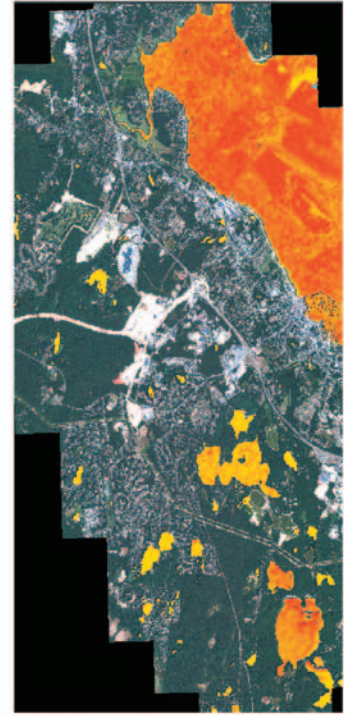
Comparisons of the two versions of the software reveals that QSC2 successfully addresses some of the principal limitations of the earlier version. The newer version eliminates the need for interactive signature derivation and the requirement for prior knowledge of water depths or water quality characteristics, without sacrificing accuracy. This is important for analyzing waters about which such knowledge is unavailable,



0.00000 - 1.99636 mg/m ³	Orange
1.99636 - 3.16516 mg/m ³	Dark Orange
3.16516 - 5.01828 mg/m ³	Light Orange
5.01828 - 7.95634 mg/m ³	Yellow-Orange
7.95634 - 12.61455 mg/m ³	Yellow
12.61455 - 20.00001 mg/m ³	Light Yellow
Over 20.00001 mg/m ³	White



0.00000 - 1.30313 g/m ³	Orange
1.30313 - 1.95880 g/m ³	Dark Orange
1.95880 - 2.94438 g/m ³	Light Orange
2.94438 - 4.42584 g/m ³	Yellow-Orange
4.42584 - 6.65270 g/m ³	Yellow
6.65270 - 10.00000 g/m ³	Light Yellow



0.00000 - 1.30313 g/m ³	Orange
1.30313 - 1.95880 g/m ³	Dark Orange
1.95880 - 2.94438 g/m ³	Light Orange
2.94438 - 4.42584 g/m ³	Yellow-Orange
4.42584 - 6.65270 g/m ³	Yellow
6.65270 - 10.00000 g/m ³	Light Yellow

Plate 3. Image-derived concentrations of suspended chlorophyll (left), suspended sediments (center), and colored dissolved organic matter (right) for the Plymouth Harbor image shown in Plate 1.



VSSR (1) (445-516 nm)

Histogram VSSR Range

0	0.0 - 1.2 meter	Yellow
590	1.2 - 1.9 meter	Light Yellow
42805	1.9 - 3.0 meter	Yellow-Orange
151350	3.0 - 4.7 meter	Light Orange
330322	4.7 - 7.4 meter	Orange
464876	7.4 - 11.5 meter	Dark Orange
106972	11.5 - 18.1 meter	Light Orange
44851	18.1 - 28.3 meter	Orange
20410	28.3 - 44.3 meter	Dark Orange
9602	44.3 - 69.3 meter	Light Orange
4313	69.3 - 108.6 meter	Orange
40462	108.6 - 170.0 meter	Dark Orange

VSSR (2) (506-595 nm)

0	0.0 - 2.7 meter	Yellow
25469	2.7 - 4.4 meter	Light Yellow
148677	4.4 - 7.1 meter	Yellow-Orange
543195	7.1 - 11.4 meter	Light Orange
319913	11.4 - 18.2 meter	Orange
109245	18.2 - 29.3 meter	Dark Orange
70054	29.3 - 47.0 meter	Light Orange

VSSR (3) (632-698 nm)

0	0.0 - 2.4 meter	Yellow
3109	2.4 - 3.5 meter	Light Yellow
97339	3.5 - 4.9 meter	Yellow-Orange
767759	4.9 - 7.0 meter	Light Orange
348346	7.0 - 10.0 meter	Orange

VSSR (4) (757-853 nm)

0	0.0 - 1.2 meter	Yellow
1216553	1.2 - 1.5 meter	Light Yellow

Plate 4. Image-derived Vertical Subsurface Sighting Range at 445 to 516 nm (Band 1 bandpass) for the Plymouth Harbor image (left). The histograms for VSSR(n) for Bands 1 through 4 are shown for comparison (right).



Histogram HSSR Range

0	0.0 - 0.5 meter	
5038	0.5 - 0.8 meter	
83340	0.8 - 1.3 meter	
157254	1.3 - 2.0 meter	
449085	2.0 - 3.2 meter	
330310	3.2 - 5.1 meter	
66364	5.1 - 8.1 meter	
37245	8.1 - 12.9 meter	
28099	12.9 - 20.6 meter	
11693	20.6 - 32.7 meter	
4605	32.7 - 52.1 meter	
3396	52.1 - 82.9 meter	
40124	82.9 - 132.0 meter	

0	0.0 - 0.7 meter
40874	0.7 - 1.2 meter
141430	1.2 - 2.0 meter
418472	2.0 - 3.2 meter
412002	3.2 - 5.3 meter
77733	5.3 - 8.8 meter
40097	8.8 - 14.4 meter
29309	14.4 - 23.7 meter
13580	23.7 - 38.9 meter
43056	38.9 - 64.0 meter

HSSR (3) (632-698 nm)

0	0.0 - 0.7 meter
10778	0.7 - 1.0 meter
84036	1.0 - 1.4 meter
163073	1.4 - 2.1 meter
395432	2.1 - 3.1 meter
374742	3.1 - 4.5 meter
72846	4.5 - 6.5 meter
50396	6.5 - 9.6 meter
65250	9.6 - 14.0 meter

HSSR (4) (757-853 nm)

0	0.0 - 0.5 meter
2768	0.5 - 0.6 meter
62318	0.6 - 0.9 meter
233697	0.9 - 1.1 meter
740063	1.1 - 1.5 meter
177707	1.5 - 2.0 meter

(a)



Turbidity (1) (445-516 nm)

Histogram Turbidity Range

0	0.022 - 0.040 1/meter	
41170	0.040 - 0.074 1/meter	
6593	0.074 - 0.137 1/meter	
18068	0.137 - 0.251 1/meter	
41610	0.251 - 0.461 1/meter	
73396	0.461 - 0.848 1/meter	
429279	0.848 - 1.558 1/meter	
454169	1.558 - 2.862 1/meter	
141441	2.862 - 5.260 1/meter	
10827	5.260 - 9.667 1/meter	

Turbidity (2) (506-595 nm)

0	0.000 - 0.072 1/meter
43215	0.072 - 0.119 1/meter
14429	0.119 - 0.197 1/meter
31411	0.197 - 0.327 1/meter
39149	0.327 - 0.540 1/meter
96711	0.540 - 0.893 1/meter
429829	0.893 - 1.477 1/meter
399151	1.477 - 2.443 1/meter
129210	2.443 - 4.041 1/meter
33448	4.041 - 6.683 1/meter

Turbidity (3) (632-698 nm)

0	0.000 - 0.350 1/meter
71829	0.350 - 0.511 1/meter
51420	0.511 - 0.746 1/meter
100688	0.746 - 1.089 1/meter
383943	1.089 - 1.590 1/meter
381613	1.590 - 2.322 1/meter
145753	2.322 - 3.390 1/meter
74319	3.390 - 4.951 1/meter
6988	4.951 - 7.230 1/meter

Turbidity (4) (757-853 nm)

0	0.000 - 2.470 1/meter
188971	2.470 - 3.088 1/meter
628621	3.088 - 3.861 1/meter
282103	3.861 - 4.827 1/meter
87689	4.827 - 6.034 1/meter
27331	6.034 - 7.543 1/meter
1838	7.543 - 9.430 1/meter

(b)

Plate 5. (a) Image-derived Horizontal Subsurface Sighting Range at 445 to 516 nm (Band 1 bandpass) for the Plymouth Harbor image (left). The histograms for $HSSR(n)$ for the Bands 1 through 4 band passes are shown for comparison (right). (b) Image-derived Turbidity at 445 to 516 nm (Band 1 band pass) for the Plymouth Harbor image (left). The histograms for Turbidity for the Bands 1 through 4 band passes are shown for comparison (right).

and it suppresses errors caused by less-than-optimal signatures and incorrect user inputs. Furthermore, the ability of QSC2 to simultaneously retrieve water composition and depth, and to adaptively compensate for errors in the LUT values (through use of SUN_{LUT}) enables more uniform accuracies to be achieved over a broader range of surface reflectance (glint), water column, bottom, and depth characteristics.

This was confirmed by a demonstration of performance of the QSC2 software using a four-band Ikonos image of Plymouth, Massachusetts. Accuracies of the image-derived compositions, water clarity, and depths were assessed using field and laboratory measurements for eight representative lakes in the scene. The means of the differences of the field-measured and image-derived suspended chlorophyll and colored dissolved organic carbon concentrations for the eight lakes were 1.82 $\mu\text{g/l}$ and 4.34 mgC/l , respectively. The image-derived concentrations of suspended sediments were all below the threshold of detection for the field samples (5 mg/l), in agreement with the field measurements. The mean of the differences between field-measured and image-derived Secchi depths (water clarity) and actual depths were 0.76 m and 0.57 m, respectively. In general, the agreement was good and uniform across the range of lakes sampled. The origins of the differences are uncertain, but are likely due primarily to the fundamental differences between the field and remote sensing measurement approaches.

A prime benefit of the output from the QSC2 software is the wide-area synoptic view of the various parameters that the software provides. The information provides spatially complete and simultaneous coverage of all water bodies in the image, in contrast to the typically non-simultaneous spot coverage provided by traditional field sampling. The output layers are two-dimensional maps of depth, water composition, and water clarity for a single point in time. This allows the spatial distribution of the various parameters to be analyzed and correlated with each other and with shoreline and inland features/phenomena without the complicating influence of temporal variability. Temporal variations of these relationships can be assessed in a controlled manner through repeat coverage over multiple dates. The patterns and changes in patterns over time (with multitemporal coverage) in the output layers provide critical insights and information about the sources and causes of phenomena responsible for the status of the water body. Agencies responsible for water quality monitoring under the Clean Water Act provisions would benefit greatly from this type of information.

Acknowledgments

The authors greatly acknowledge the contributions of Brad Thomson, Melanie Harlow, and Dr. John Mustard of the NASA Affiliated Research Center at Brown University. The Ikonos imagery used in this study was provided to GeoSyntec as part of a different project and its purchase was funded by the NASA ARC Program. The authors would also like to thank the following parties for their integral role in this research: the Massachusetts Watershed Initiative, EPA Alpha Analytical Labs, Region 1 Laboratories, U.S. Environmental Rental Corporation, Aquatic Control Technologies, and GeoLabs Inc, for support and assistance with laboratory analysis. Portions of this work were supported by internal research and development funds by both Applied Analysis Incorporated of Billerica, Massachusetts and GeoSyntec Consultants.

References

Bukata, R.P., J.H. Jerome, J.E. Bruton, S.C. Jain, and H.H. Zwick, 1981. Optical water quality model of Lake Ontario. 1. Determination of the optical cross sections of organic and inorganic particulates in Lake Ontario, *Applied Optics*, 20:1696–1703.

- Bukata, R.P., J.H. Jerome, and J.E. Bruton, 1988. Relationships among Secchi disk depth, beam attenuation coefficient, and irradiance attenuation coefficient for Great Lakes waters, *Journal of Great Lakes Research*, 14:347–355.
- Bukata, R.P., J.H. Jerome, K.Ya. Kondratyev, and D.V. Pozdnyakov, 1995. *Optical Properties and Remote Sensing of Inland and Coastal Waters*, CRC Press, Inc., Boca Raton, Florida, 362 p.
- Carder, K.L., F.R. Chen, Z.P. Lee, S.K. Hawes, and D. Kamykowski, 1999. Semianalytic Moderate-Resolution Imaging Spectrometer algorithms for chlorophyll a and absorption with bio-optical domains based on nitrate-depletion temperatures, *Journal of Geophysical Research*, 104:5403–5421.
- Cipollini, P.G., G. Corsini, M. Diani, and R. Grasso, 2001. Retrieval of sea water optically active parameters from hyperspectral data by means of generalized radial basis function neural networks, *IEEE Transactions on Geoscience and Remote Sensing*, 39:1508–1524.
- Clark, R.K., T.H. Fay, and C.L. Walker, 1987. Bathymetry calculations with Landsat 4 Thematic Mapper under a generalized ratio assumption, *Applied Optics*, 26:1134–1135.
- Dierssen, H.M., and R.C. Smith, 1997. Estimation of irradiance just below the air-water interface, *Proceedings Ocean Optics XIII*, (S. Ackelson and R. Frovin, editors) (*SPIE*, 22 October 1996, Halifax, Nova Scotia, Canada, Bellingham, Washington), 2963:204–209.
- , 2000. Bio-optical properties and remote sensing ocean color algorithms for Antarctic Peninsula waters, *Journal of Geophysical Research*, 105:26,301–26,312.
- DiToro, D.M., 1978. Optics of turbid estuarine waters: Approximations and applications, *Water Research*, 12:1059–1068.
- Flanagan, M., and D.L. Civco, 2001. IMAGINE Subpixel Classifier Version 8.4, *Photogrammetric Engineering & Remote Sensing*, 67:23–28.
- Garver, S.A., and D.A. Siegel, 1997. Inherent optical property inversion of ocean color spectra and its biogeochemical interpretation. I. Time series from the Sargasso Sea, *Journal of Geophysical Research*, 102:18,607–18,625.
- Gordon, H.R., O.B. Brown, and M.N. Jacobs, 1975. Computed relationships between the inherent and apparent optical properties of a flat homogeneous ocean, *Applied Optics*, 14:417–427.
- Gordon, H.R., O.B. Brown, R.H. Evans, J.W. Brown, R.C. Smith, K.S. Baker, and D.K. Clark, 1988. A semi-analytic radiance model of ocean color, *Journal of Geophysical Research*, 93:10,909–10,924.
- Huguenin, R.L., M.A. Karaska, D. Van Blaricom, B. Savitsky, and J.R. Jensen, 1997a. Subpixel classification of Bald Cypress and Tupelo Gum trees in Thematic Mapper imagery, *Photogrammetric Engineering & Remote Sensing*, 63:717–725.
- Huguenin, R.L., E.R. Boudreau, and M.A. Karaska, 1997b. An adaptation of the AASAP subpixel Analysis Software for Automated Bathymetry Mapping, *Proc. of Fourth International Conference on Remote Sensing for Marine and Coastal Environment*, 17–19 March, Orlando, Florida (ERIM, Ann Arbor, Michigan), 1:308–316.
- Huguenin, R.L., M. Wang, M.A. Karaska, and K.E. Roberts, 1998. Automated scene-derived normalization of spectral imagery for subpixel classification, *Imaging Spectrometry IV* (Michael R. Descour, and Sylvia S. Shen, editors), (*SPIE*, 20–21 July, San Diego, California, Bellingham, Washington), 3438:157–161.
- Jerome, J.H., R.P. Bukata, and J.E. Bruton, 1988. Utilizing the components of vector irradiance to estimate the scalar irradiance in natural waters, *Applied Optics*, 21:4012–4018.
- Kalle, K., 1966. The problem of the gelbstoff in the sea, *Oceanography and Marine Biology Annual Reviews*, 43:91–104.
- Karaska, M.A., R.L. Huguenin, J.L. Beacham, M. Wang, J.R. Jensen, and R.S. Kaufmann, 2004. AVIRIS measurements of chlorophyll, suspended minerals, dissolved organic carbon, and turbidity in the Neuse River, North Carolina, *Photogrammetric Engineering & Remote Sensing*, 70(1):125–133.
- Kirk, J.T.O., 1984. Dependence of relationship between inherent and apparent optical properties of water on solar altitude, *Limnology and Oceanography*, 29:350–356.
- , 1991. Volume scattering function, average cosines, and the underwater light field, *Limnology and Oceanography*, 36: 455–467.

- LaPotin, P., R. Kennedy, T. Pangburn, and R. Bolus, 2001. Blended spectral classification techniques for mapping water surface transparency and chlorophyll concentration, *Photogrammetric Engineering & Remote Sensing*, 67:1059–1065.
- Lee, Z.P., K.L. Carder, C. Mobley, R.G. Steward, and J.S. Patch, 1999. Hyperspectral remote sensing for shallow waters, 2. Deriving bottom depths and water properties by optimization, *Applied Optics*, 38:3831–3843.
- Lee, Z.P., K.L. Carder, R.F. Chen, and T.G. Peacock, 2001. Properties of the water column and bottom derived from Airborne Visible Infrared Imaging Spectrometer (AVIRIS) data, *Journal of Geophysical Research*, 106:11639–11651.
- Lyzenga, D.R., 1978. Passive remote sensing techniques for mapping water depth and bottom features, *Applied Optics*, 17:379–383.
- , 1981. Remote sensing of bottom reflectance and water attenuation parameters in shallow water using aircraft and Landsat data, *International Journal of Remote Sensing*, 2:71–82.
- , 1985. Shallow-water bathymetry using combined lidar and passive multispectral scanner data, *International Journal of Remote Sensing*, 6:115–125.
- Maritorena, S., D.A. Siegel, and A.R. Peterson, 2002. Optimization of a semi-analytical ocean color model for global-scale applications, *Applied Optics*, 41:2705–2714.
- Mausel, P.W., M.A. Karaska, C.Y. Mao, D.E. Escobar, and J.H. Everitt, 1991. Insights into secchi transparency through computer analysis of aerial multispectral video data, *International Journal of Remote Sensing*, 12:2485–2492.
- Morel, A., and B. Gentili, 1991. Diffuse reflectance of oceanic waters: Its dependence on sun angle as influenced by the molecular scattering contribution, *Applied Optics*, 30:4427–4438.
- , 1993. Diffuse reflectance of oceanic waters, II, Bidirectional aspects, *Applied Optics*, 32:6864–6879.
- Mueller, J.L., R.S. Fraser, S.F. Biggar, K.J. Thome, P.N. Slater, A.W. Holmes, R.A. Barnes, C.T. Weir, D.A. Siegel, D.W. Menzies, A.F. Michaels, and G. Podesta, 1995. Comparison of irradiance immersion coefficients for several marine environmental radiometers (MERS), *Case Studies for SeaWiFS Calibration and Validation, Part 3, Vol. 27*, (S.B. Hooker, E.R. Firestone, and J.G. Acker, editors), NASA Tech. Memo. 104566, NASA Goddard Space Flight Center, Greenbelt, Maryland, 46 p.
- O'Neill, N.T., and J.R. Miller, 1989. On calibration of passive optical bathymetry through depth soundings analysis and treatment of errors resulting from the spatial variation of environmental parameters, *International Journal of Remote Sensing*, 10:1481–1501.
- O'Reilly, J.E., S. Maritorena, B.G. Mitchell, D.A. Siegel, K.L. Carder, S.A. Garver, M. Kahru, and C.R. McClain, 1998. Ocean color chlorophyll algorithms for SeaWiFS, *Journal of Geophysical Research*, 103:24937–24953.
- Philpot, W.D., 1989. Bathymetric mapping with passive multispectral imagery, *Applied Optics*, 28:1569–1578.
- Polcyn, F.C., W.L. Brown, and I.J. Sattinger, 1970. The measurement of water depth by remote sensing techniques, *Rep. 8973-26-F*, Willow Run Laboratory, University of Michigan, Ann Arbor, Michigan, 53 p.
- Pickard, G.L., and W.J. Emery, 1982. *Descriptive Physical Oceanography, An Introduction*, Pergamon Press, Oxford, U.K., 249 p.
- Reynolds, R.A., D. Stramski, and B.G. Mitchell, 2001. A chlorophyll-dependent semianalytical reflectance model derived from field measurements of absorption and backscattering coefficients within the Southern Ocean, *Journal of Geophysical Research*, 106:7125–7138.
- Ruddick, K.G., H.J. Gons, M. Rijkeboer, and G. Tilstone, 2001. Optical remote sensing of chlorophyll a in case 2 waters by use of an adaptive two-band algorithm with optimal error properties, *Applied Optics*, 40:3575–3585.
- Smith, R.C., and K.S. Baker, 1986. Analysis of ocean optical data II, *Ocean Optics VIII, (SPIE, 31 March–02 April, Orlando, Florida, Bellingham, Washington)*, 637:95–107.
- Thormahlen, I., J. Straub, and U. Grigul, 1985. Refractive index of water and its dependence on wavelength, temperature, and density, *Journal of Physical and Chemical Reference Data*, 14:933.
- Walker, C.L., R.K. Clark, and T.H. Fay, 1990. Shallow water bathymetry models using multispectral digital data, *Journal of Imaging Technology*, 16:170–175.
- Zhang, M.R., K.L. Carder, Z.P. Lee, F.E. Muller-Karger, and D.B. Goldgof, 1999. Noise reduction and atmospheric correction for coastal applications of Landsat Thematic mapper imagery, *Remote Sensing of Environment*, 70:167–180.